

Control over Molecular Orbital Gating and Marcus Inverted Charge Transport in Molecular Junctions with Conjugated Molecular Wires

Christian A. Nijhuis,* Ziyu Zhang, Francis Adoah, Cameron Nickle, Senthil Kumar Karuppannan, Lejia Wang, Li Jiang, Anton Tadich, Bruce Cowie, Teddy Salim, Dong-Chen Qi, Damien Thompson,* and Enrique Del Barco*

Recently it is discovered that molecular junctions can be pushed into the Marcus Inverted region of charge transport, but it is unclear which factors are important. This paper shows that the mechanism of charge transport across molecular wires can be switched between the normal and Marcus Inverted regions by fine-tuning the molecule–electrode coupling strength and the tunneling distance across oligophenylene ethynylene (OPE) wire terminated with ferrocene (Fc) abbreviated as S-OPE_nFc ($n = 1–3$). Coherent tunneling dominates the mechanism of charge transport in junctions with short molecules ($n = 1$), but for $n = 2$ or 3 redox reactions become important. By weakening the molecule–electrode interaction by interrupted conjugation, S-CH₂-OPE_nFc, intramolecular orbital gating can occur pushing the junctions completely into the Marcus Inverted region. These results indicated that weak molecule–electrode coupling is important to push junctions into the Marcus Inverted Region.

1. Introduction

Achieving control over charge transport (CT) between molecules and electrode surfaces is fundamental for the creation of new device materials in areas ranging from organic electronics^[1] and catalysis^[2,3] to energy management^[4] and biology.^[5] For this reason, it is important to study the mechanisms of CT across molecule–electrode interfaces in detail. Molecular junctions make it possible to study the mechanisms of CT at the smallest possible length-scale under very well-controlled conditions giving unprecedented insights into, for example, thermoelectric properties,^[6] light–matter interactions,^[7] and switching mechanisms.^[8] Recently, the

C. A. Nijhuis, Z. Zhang, S. K. Karuppannan, L. Jiang
Department of Chemistry
National University of Singapore
3 Science Drive 3, Singapore 117543, Singapore
E-mail: c.a.nijhuis@utwente.nl

C. A. Nijhuis
Department of Molecules and Materials
MESA+ Institute for Nanotechnology
Center for Brain-Inspired Nano Systems and Molecules Center
Faculty of Science and Technology
University of Twente
P.O. Box 217, 7500 AE Enschede, The Netherlands

F. Adoah, C. Nickle, E. D. Barco
Department of Physics
University of Central Florida
Orlando, Florida 32816, USA
E-mail: delbarco@physics.ucf.edu

 The ORCID identification number(s) for the author(s) of this article can be found under <https://doi.org/10.1002/aelm.202200637>.

© 2022 The Authors. Advanced Electronic Materials published by Wiley-VCH GmbH. This is an open access article under the terms of the Creative Commons Attribution License, which permits use, distribution and reproduction in any medium, provided the original work is properly cited.

DOI: 10.1002/aelm.202200637

L. Wang
School of Materials and Chemical Engineering
Ningbo University of Technology
Fenghua Rd 201, Ningbo, Zhejiang 315211, P.R. China

A. Tadich, B. Cowie
Australian Synchrotron Clayton
Victoria 3168, Australia

T. Salim
School of Materials Science and Engineering
Nanyang Technological University
50 Nanyang Avenue, Singapore 639798, Singapore

D.-C. Qi
Centre for Materials Science
School of Chemistry and Physics
Queensland University of Technology
Brisbane, Queensland 4001, Australia

D. Thompson
Department of Physics
Bernal Institute
University of Limerick
Limerick V94 T9PX, Ireland
E-mail: Damien.Thompson@ul.ie

Marcus Inverted region (MIR) for CT has been found in redox-active molecular devices where charges traverse electrode–molecule–electrode junctions via incoherent tunneling (also called hopping) without a noticeable thermally activated component (activation energy, E_a) to cross the hopping barrier.^[9,10] Unlike redox processes in solution,^[11] in junctions the energy from the leads compensates for E_a . Recently, it has been shown that this elimination of E_a in the MIR can be used to improve the performance of molecular devices.^[12] Incoherent tunneling has been frequently observed in molecular junctions but MIR has been only recently reported for a very few systems^[9,10,12,13] and it remains unclear which factors push molecular junctions into MIR because the mechanism of CT depends on several intertwined factors. Here we show that MIR can be turned on and off by varying the coupling strength of the molecule with the electrode (via the insertion of a single methylene $-\text{CH}_2-$ unit) which works only for junctions with long, redox-active molecular wires. On the other hand, coherent tunneling dominates in short wires. Unraveling the interplay between molecular length and molecule–electrode coupling strength and understanding how this interplay affects the mechanism of CT (incoherent vs coherent tunneling) is important for future designs of molecular junctions.

In essence, the Landauer and Marcus theories describe CT at the two opposite ends of the spectrum. The Landauer–Buttiker theory describes coherent tunneling and is widely used to model current flow across molecular junctions with high coupling factor between the molecules and electrodes.^[14,15] The Marcus theory describes incoherent tunneling (also called hopping) and is widely used to explain incoherent redox processes in solution.^[18,19] In molecular tunnel junctions, in principle both processes can take place but it is still poorly understood when a junction transits from coherent to incoherent tunneling because of the difficulty to disentangle the factors. As we show here, molecular length, molecule–electrode coupling strength, and applied voltage all affect the CT mechanism.

The Landauer–Buttiker model works very well for short molecules with strong molecule–electrode coupling, but in this work, we show that for molecules with increasing length and decreasing molecule–electrode coupling (low γ), redox-reactions become important, and the Landauer model alone is not suitable.

For junctions where redox processes in the molecules cannot be ignored, such as in this work, alternative theories involving the Marcus theory have been proposed that describe incoherent redox processes in solid-state junctions that lack an electrolyte.^[20–22] Migliore and Nitzan developed a model combining Marcus and Landauer theories that successfully explains CT in junctions where the relative distance between the Marcus parabolas is affected by electrical gating between the involved charge states. They achieved this by decoupling the slow redox transitions between the neutral (M) and charged (M^+) states of a molecule inside junctions (modeled by the Marcus theory) from the fast sequential tunneling of electrons/holes between the electrodes and the respective molecular charge states (modeled by the Landauer theory).^[23] According to this model, Equations 1 and 2 describe the transport rates to ($K_{M \rightarrow M^+}$) and from ($K_{M^+ \rightarrow M}$) the charged states.

$$K_{M \rightarrow M^+} = \frac{1}{\sqrt{4\pi\lambda k_B T}} \int dE \Gamma(E) e^{-\frac{(\Delta E + E - \lambda)^2}{4\lambda k_B T}} f(E) \quad (1)$$

$$K_{M^+ \rightarrow M} = \frac{1}{\sqrt{4\pi\lambda k_B T}} \int dE \Gamma(E) e^{-\frac{(\Delta E + E - \lambda)^2}{4\lambda k_B T}} [1 - f(E)] \quad (2)$$

Here $\Gamma(E)$ is the tunneling rate between the molecular state and the electrodes, $\Delta E = \Delta E_0 + \mu$ is the electrochemical potential of the electrodes where ΔE_0 is the energy difference between the two molecular states ($\Delta E_0 = E_M(x_M) - E_{M^+}(x_{M^+})$), x_M and x_{M^+} are the molecular configurations at the equilibrium of M and M^+ where x is the reaction coordinate, μ is the electrochemical potential of the leads, and λ is the reorganization energy. The model allows the inclusion of an internal electrical gating potential which affects the activation-free energies of the fluctuation probabilities of x_M and x_{M^+} and thereby shifts the relative energy position of the Marcus parabolas of the initial and the final states with respect to one another, leading to an effective change in the activation energy E_a . This internal gating results from the interaction between the different charge states of the molecule as the charge inside the molecule increases with increasing bias. This effective gating potential is directly proportional to the charge in the molecule (which depends on bias) and capacitive coupling between the two charge states. It can be written as $V_g = Q(V)/C_C$ ($\Delta E(V_g) - \lambda = 0$, $\Delta E(V_g) + \lambda = 0$). Here Q represents the bias-dependent electron charge on the molecule and capacitance C_C represents the effective capacitive coupling between the donor and the acceptor which is independent of V but determined by the molecular structure. The activation energy E_a , is given by Equation (3) and is thus dependent on V_g .

$$\frac{E_a}{k_B T} = T \frac{\partial}{\partial T} \ln(K_{M \rightarrow M^+} + K_{M^+ \rightarrow M}) \quad (3)$$

Molecular junctions that operate in MIR are very rare and it is unclear under which conditions junctions operate in MIR or Marcus normal regions. The vast majority of known redox-active molecular junctions operate in the Marcus normal region, but, as exemplified in our previous work, in junctions with a donor-bridge-acceptor (D-b-A) compound, specifically $\text{S-CH}_2\text{-DPA-(CH}_2)_n\text{-Fc}$ ($n = 1-3$, DPA = diphenylacetylene and Fc = ferrocene), charges can hop from the donor (Fc) to the acceptor (DPA).^[9] During this hopping process, the Fc units are charged, Fc^+ , resulting in a lowering of the energy of the acceptor level with respect to that of the donor due to intramolecular orbital gating. **Figure 1c** illustrates this effect in terms of Marcus parabolas for charge transfer from the donor to the acceptor and shows that for sufficiently large intramolecular orbital gating, the parabola of the initial (neutral) state Fc-DPA intersects one of the final (zwitterionic) state $\text{Fc}^+\text{-DPA}^-$ at its minimum producing barrierless charge transport. Beyond this point, the system enters the MIR and nonzero E_a is restored which in principle should slow down the electron transfer rates, but in molecular junctions this energy penalty is compensated by the energy from the electrodes. Recently, we showed that the Marcus parabolas can be shifted with respect to each other because the different charge states of a redox molecule interact differently with the applied electric field.^[10] This mechanism

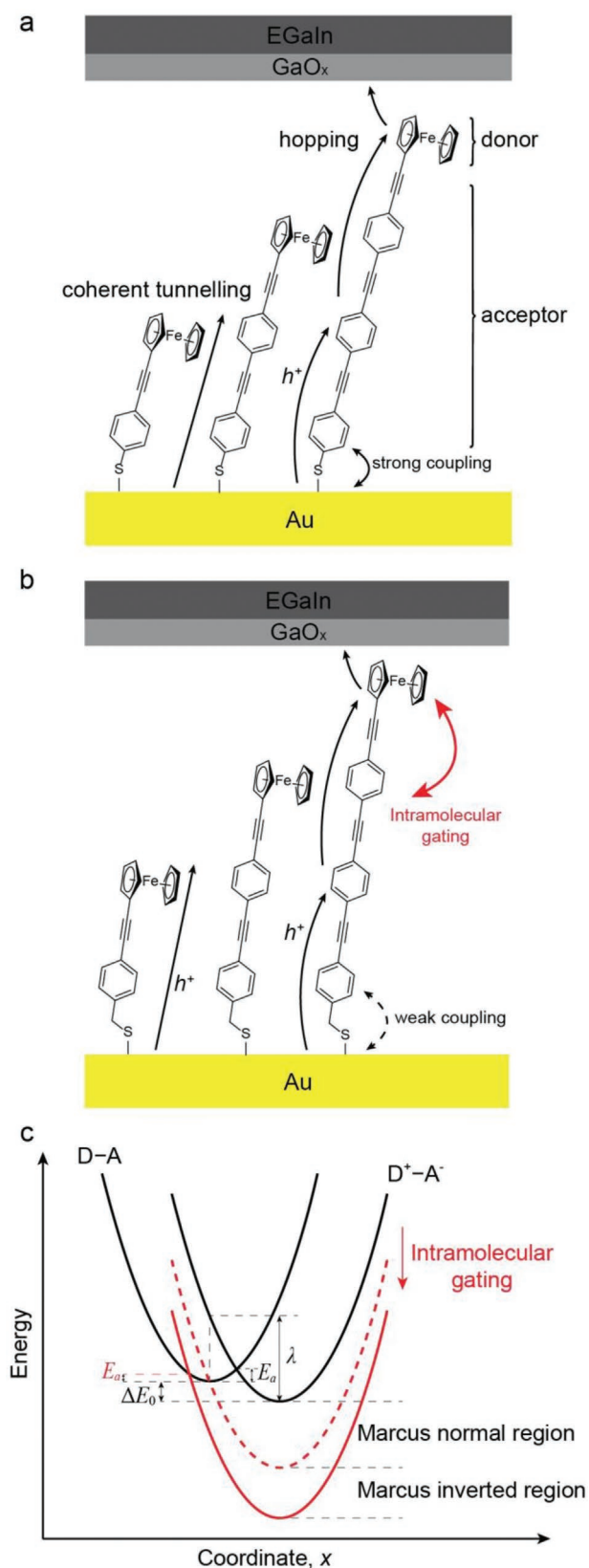


Figure 1. Schematic illustration of the junctions (a) Au-S-OPE_nFc//GaO_x/EGaIn ($n = 1-3$) and (b) Au-S-CH₂-OPE_nFc//GaO_x/EGaIn ($n = 1-3$). EGaIn stands for eutectic gallium-indium alloy and GaO_x represents

can also explain the results of Kang et al.^[24] who observed MIR for a molecule with only an electron acceptor group. However, for all these examples the mechanism of charge transport strongly depends on the intertwined factors of the molecule-electrode coupling strength (γ) and the molecular length (d) and so it remains unclear why they operate in the MIR instead of the Marcus normal region.

In this work, we address the question of how MIR can be accessed in molecules where the donor and acceptor groups are fully conjugated and, in principle, intramolecular orbital gating strength should be strong enough to observe MIR. A fully conjugated molecular wire may couple too strongly to the electrodes resulting in coherent, rather than incoherent, tunneling diminishing MIR. To investigate the role of both γ and d in the mechanism of CT of redox-molecules operating in the Marcus Inverted region, we incorporated a conjugated oligophenylene ethynylene (OPE) of variable length functionalized with Fc, S-(Ph-C≡C)_n-Fc (S-OPE_nFc, $n = 1-3$), or alternatively a molecular wire with an interrupted conjugation at the thiol anchoring group S-CH₂-(Ph-C≡C)_n-Fc (S-CH₂-OPE_nFc, $n = 1-3$), in EGaIn junctions (Figure 1). Thus, we control γ via the -CH₂- moiety and d via n . The major conclusion of this work is that with a single -CH₂- unit we can reduce γ enough to push the molecular junctions into the MIR, but only for junctions with $n > 1$. Junctions lacking the -CH₂- unit, and those with short molecules ($d < 1.5$ nm for $n = 1$), remain in the strong coupling regime where coherent tunneling dominates the mechanism of charge transport.

2. Results and Discussion

2.1. Characterization of the Monolayers

To characterize both the electronic and supramolecular structure of the SAMs, we used a range of characterization techniques (see Section S1–S7, Supporting Information) and the SAM properties are summarized in **Table 1**. From these results, we make the following observations. i) The surface coverages determined by cyclic voltammetry (CV) are within error the same for all OPE derivatives and are significantly higher than the previously reported value for S-OPE₁Fc monolayers on Au electrode (1.2×10^{-10} mol cm⁻²)^[26] but lower than for SAMs made of only OPE units (9.7×10^{-10} mol cm⁻²).^[27] ii) The monolayer thickness d_{SAM} determined from angle-resolved X-ray photoemission spectroscopy (XPS) scales with the number of OPE units. The S-CH₂-OPE_nFc monolayers are 2–3 Å thicker than S-OPE_nFc monolayers with the same n due to the extra -CH₂- unit. iii) The energy of the HOMO (E_{HOMO}), determined by

the 0.7–1.0 nm-thick gallium oxide layer.^[25] The straight arrow indicates coherent tunneling and the curved arrows indicate incoherent tunneling (or hopping). The double arrows indicate the strong (solid black) and weak (dashed black) coupling between OPE and the Au electrode, and the intramolecular orbital gating (red) between the donor D (Fc) and acceptor A (OPE). c) The Marcus parabolas for the electron transfer between Fc and OPE. The red arrow indicates the intramolecular orbital gating effect, which moves the parabola of the D⁺-A⁻ state down into the activationless (dashed red line) and then the Marcus Inverted regime (solid red line).

Table 1. Properties of the self-assembled monolayers.

SAM	CV ^{a)}			UPS ^{b)}			XPS ^{c)}		NEXAFS ^{d)}		UV-Vis ^{e)}		
	ρ_{SAM} [$\times 10^{-10}$ mol cm ⁻²]	$E_{\text{HOMO-CV}}$ [eV]	FWHM- E_{pa} [mV]	Φ_{SAM} [eV]	$\delta E_{\text{ME,H}}$ [eV]	$E_{\text{HOMO-UPS}}$ [eV]	d_{SAM} [Å]	ρ_{rel}	$\alpha(^{\circ})$	E_{LUMO} [eV]	$\delta E_{\text{ME,L}}$ [eV]	E_{g} [eV]	$E_{\text{LUMO-UV}}$ [eV]
S-OPE ₁ Fc	3.5 ± 0.13	-5.12 ± 0.01	140 ± 5	4.44	0.66	-5.10	13 (11.5)	1.1	34	-2.51	1.93	3.13	-1.97
S-OPE ₂ Fc	3.86 ± 0.08	-5.13 ± 0.01	123 ± 1	4.38	0.77	-5.15	17 (16.5)	1.3	33	-2.58	1.80	3.05	-2.1
S-OPE ₃ Fc	3.4 ± 0.11	-5.16 ± 0.01	137 ± 2	4.35	0.82	-5.17	23 (20.4)	1.2	35	-2.63	1.72	3.01	-2.16
S-CH ₂ -OPE ₁ Fc	3.6 ± 0.21	-5.10 ± 0.01	218 ± 10	4.38	0.72	-5.10	15 (13.6)	1.1	30	-2.43	1.95	3.16	-1.94
S-CH ₂ -OPE ₂ Fc	3.4 ± 0.14	-5.17 ± 0.01	207 ± 6	4.29	0.85	-5.14	22 (20.3)	1.0	25	-2.46	1.83	3.03	-2.11
S-CH ₂ -OPE ₃ Fc	3.7 ± 0.12	-5.17 ± 0.01	217 ± 14	4.26	0.91	-5.17	25 (25.5)	1.1	26	-2.63	1.63	2.99	-2.18

^{a)} ρ_{SAM} is the surface coverage. $E_{\text{HOMO-CV}}$ is the HOMO energy level calculated from the anodic peak potential. The error bars represent standard deviation from three independent measurements; ^{b)} Φ_{SAM} is the SAM work function, δE_{ME} is the offset between HOMO and the Fermi level and $E_{\text{HOMO-UPS}}$ is the HOMO level with respect to vacuum. The error is 50 meV, the step size for the spectra; ^{c)} d_{SAM} is the SAM thickness. The error is 2 Å, estimated from 10% variance in peak fitting. The value in parentheses is thickness derived from CPK models and α . ρ_{rel} is the relative surface coverage (using S-CH₂-OPE₂Fc as reference); ^{d)} α is the tilt angle of the Fc-OPE plane to the surface normal. The error is 2°, estimated from the linear fitting error of peak intensities against the incident angles. E_{LUMO} is calculated from the photon energy of the first peak in NEXAFS and the binding energy of the corresponding C 1s peak; ^{e)} E_{g} is the optical HOMO–LUMO gap. The error is 30 meV, estimated from the step size of UV-vis spectra. $E_{\text{LUMO-UV}}$ is the LUMO level calculated from E_{g} and $E_{\text{HOMO-UPS}}$.

ultraviolet photoemission spectroscopy (UPS), is within error the same for all derivatives, but the shift of E_{HOMO} with respect to E_{F} , $\delta E_{\text{ME,H}} = E_{\text{HOMO}} - E_{\text{F}}$, increases with n . iv) The optical HOMO-LUMO gap, $E_{\text{g,0}}$, determined with UV-Vis spectroscopy, decreases with n . Consequently, the energy of the LUMO, $E_{\text{LUMO-UV}}$, decreases with increasing n . v) The decrease of $\delta E_{\text{ME,L}} = E_{\text{LUMO}} - E_{\text{F}}$, was verified with near-edge X-ray absorption fine structure (NEXAFS) spectroscopy. vi) The tilt angle of the SAM with respect to the surface normal is 4–9° smaller for the S-CH₂-OPE _{n} Fc SAMs than for the S-OPE _{n} Fc SAMs. From these observations, we conclude that all SAMs form dense monolayers with the molecules in an upright position with a very similar overall supramolecular structure of the SAMs except that S-CH₂-OPE _{n} Fc SAMs are less tilted (and therefore more ordered) than S-OPE _{n} Fc SAMs. The overall electronic structure of all the SAMs is remarkably similar but $\delta E_{\text{ME,L}}$ decreases by ≈ 200 meV, and $\delta E_{\text{ME,H}}$ increases by roughly 200 meV with increasing n (Figure S33, Supporting Information).

To elucidate in more detail how both types of SAMs couple to the Au surface, we performed density functional theory (DFT) calculations. **Figure 2e** shows that for S-OPE₁Fc, the LUMO is completely delocalized with contributions from the Fc, OPE, sulfur, and metal. By contrast, in S-CH₂-OPE₁Fc, the CH₂ linker has almost no contribution to the LUMO and breaks the conjugation between OPE and the metal surface. Based on this result, we conclude that S-OPE _{n} Fc and S-CH₂-OPE _{n} Fc SAMs can be considered as strongly and weakly coupled SAMs. In addition, the calculations show the HOMO of the systems are localized on the iron atom in Fc (Figure 2f) with minor contributions from the sulfur atom. For more details, see Figure S29–S32, Supporting Information. Thus, these SAMs are highly asymmetrical and are potential rectifiers analogous to ferrocenylalkanethiolates.^[28]

Since these monolayers are new, we discuss their electrochemical behavior in more detail. Peak deconvolution (Figure 2c,d) shows that the cyclic voltammograms are dominated by the main peak representing the Fc groups in a well-packed SAM. Only a small post-peak that likely originates from physisorbed molecules is present, similar to what we have reported for ferrocenylalkanethiolate SAMs.^[29] The contribution of this post-peak diminishes with increasing n indicating that long molecules form better-packed SAMs than short molecules, likely due to the larger supramolecular OPE– π – π network for long molecules. The peak oxidation potential is very similar for all SAMs (Table 1). Interestingly, the full width at half maximum (FWHM) values for the main anodic peak are 123–140 meV for S-OPE _{n} Fc and 207–218 meV for S-CH₂-OPE _{n} Fc, both of which are higher than the theoretical value for a homogeneous monolayer (90 meV)^[30] and the reported well-packed ferrocenylalkanethiolate SAMs.^[31] In the context of the Laviron analysis,^[32,33] broadening of the peaks in CV can be related to repulsive molecule–molecule interactions. Therefore, we conclude that the large FWHM values in S-CH₂-OPE _{n} Fc SAMs are caused by the strong repulsion between Fc groups when they are charged during oxidation.^[34] The rigid OPE units give less freedom for the Fc groups to rearrange and lead to stronger repulsion compared to ferrocenylalkanethiolate SAMs.^[35] This interpretation implies that the repulsion between charged Fc units is stronger in S-CH₂-OPE _{n} Fc than S-OPE _{n} Fc SAMs which agrees with the more-ordered neutral SAM structures for S-CH₂-OPE _{n} Fc compared to S-OPE _{n} Fc as deduced from the measured smaller tilt angles (Table 1) and the measured higher rectification ratios (associated with lower leakage currents) for S-CH₂-OPE _{n} Fc compared to S-OPE _{n} Fc (see next section).

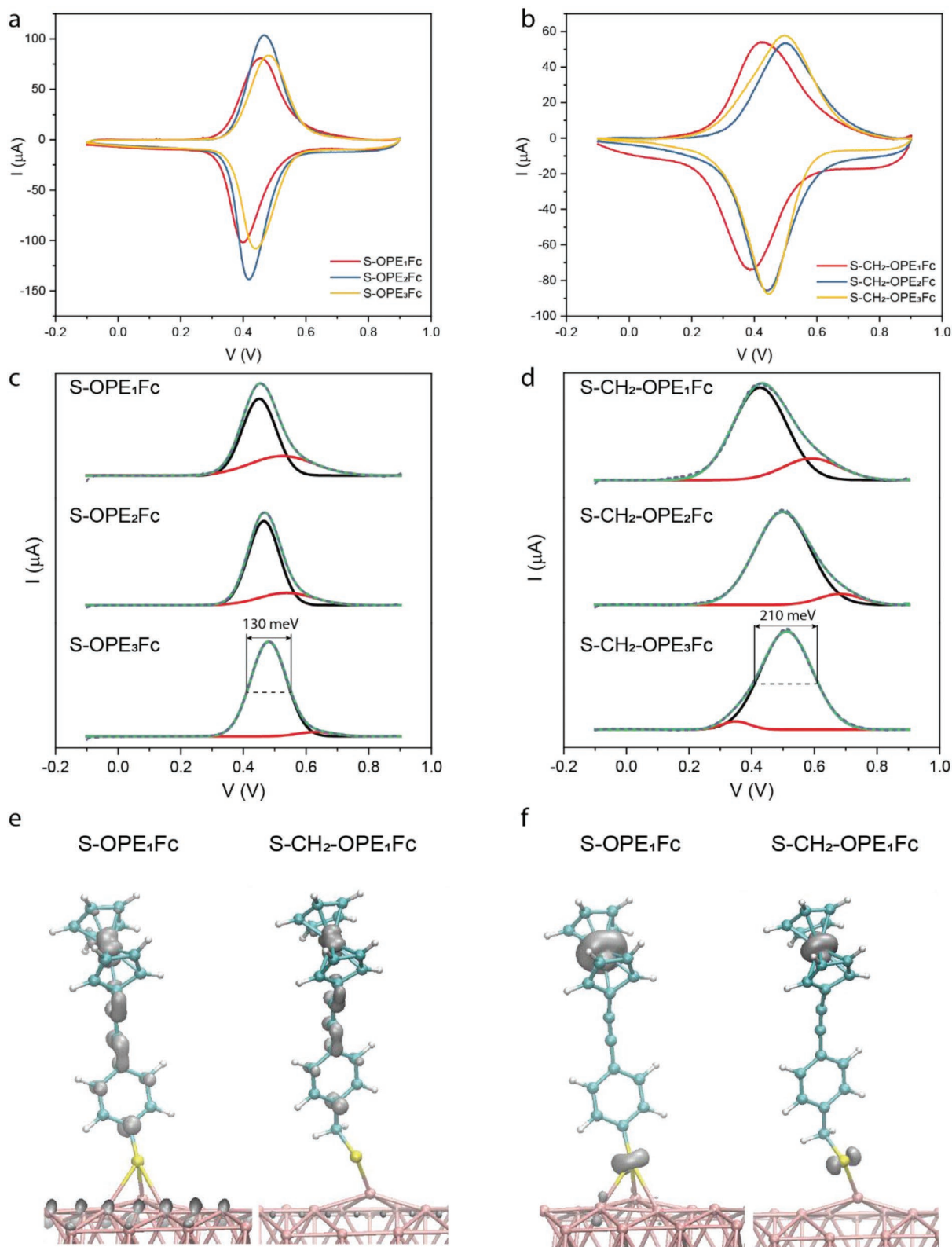


Figure 2. Cyclic voltammograms of a) S-OPE_nFc and b) S-CH₂-OPE_nFc measured at a scan rate of 1 V s^{-1} using a platinum counter electrode, an Ag/AgCl reference electrode and 1.0 M HClO_4 solution as the electrolyte. Deconvolution of the anodic peaks of c) S-OPE_nFc and d) S-CH₂-OPE_nFc, with all peaks fitted to a Gaussian function. Calculated electron density surface for e) the LUMO of S-OPE₁Fc and S-CH₂-OPE₁Fc, and f) the HOMO of S-OPE₁Fc and S-CH₂-OPE₁Fc. All surfaces in panels e and f are visualized with the same isovalue of 0.05 atomic units. The full DFT dataset and details of the DFT methods are given in Section S10, Supporting Information.

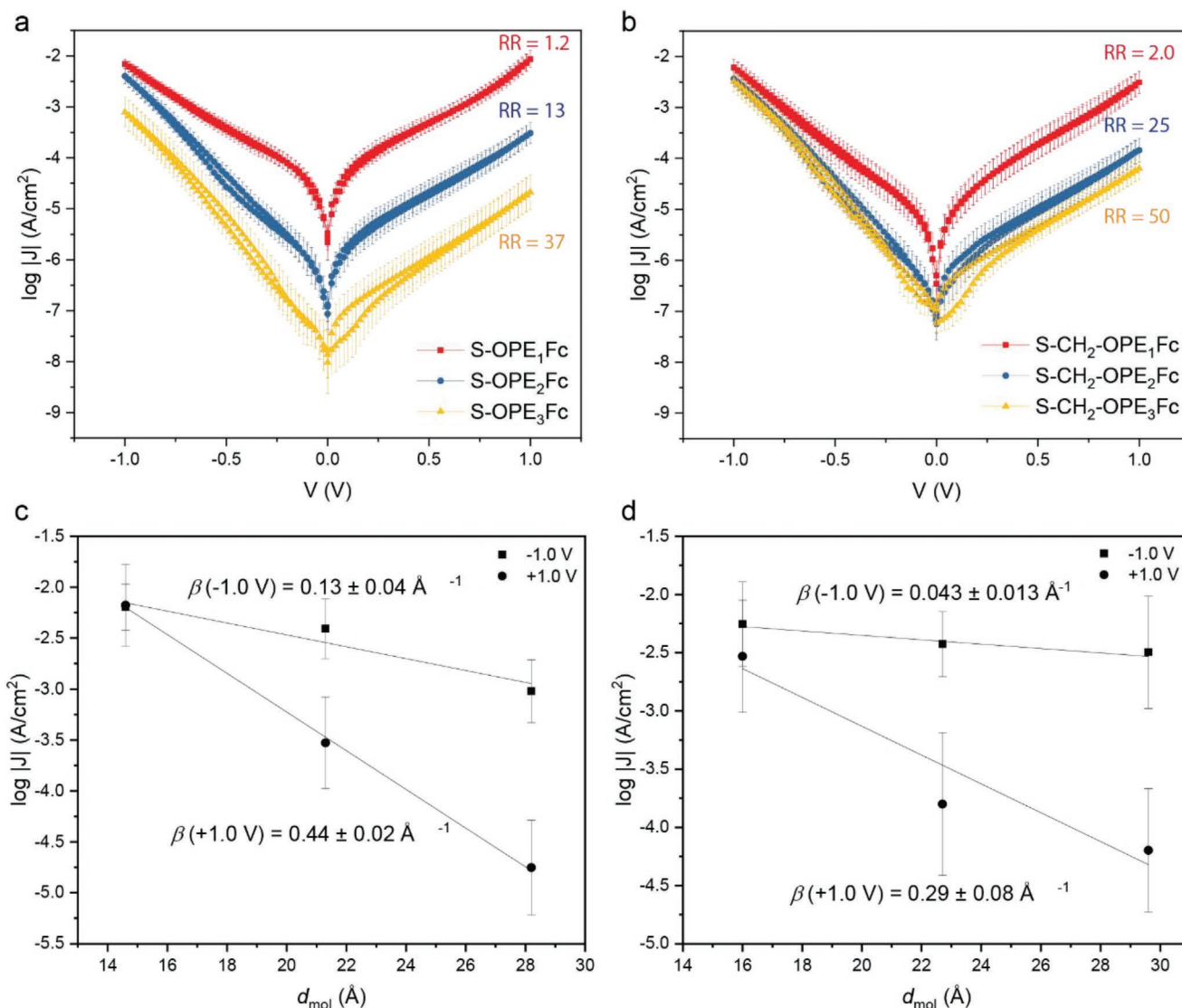


Figure 3. The values of $\langle \log_{10}|J \rangle_C$ as a function of V for junctions of a) Au/S-OPE_nFc//GaO_x/EGaIn and b) Au/S-CH₂-OPE_nFc//GaO_x/EGaIn. The error bars represent the 95% confidence intervals from 400–460 data points (Table S3, Supporting Information). The current density at -1.0 V (squares) and $+1.0$ V (circles) as a function of d_{mol} for c) S-OPE_nFc and d) S-CH₂-OPE_nFc; solid lines are fits to Equation 5 (below).

2.2. Diode Characteristics

We formed electrical contacts to the SAMs with cone-shaped tips of GaO_x/EGaIn following a previously reported method.^[36,37] These junctions are stable in the bias window of -1 V to $+1$ V with $\sim 84\%$ yield of nonshorting, stable junctions (108 out of 129 junctions, Table S3, Supporting Information). **Figure 3a,b** shows the Gaussian mean values of $\log_{10}|J|$, $\langle \log_{10}|J \rangle_C$ as a function of the applied bias voltage V (see Figure S21, Supporting Information for the heat maps of all $J(V)$ data). The rectification ratios $RR \equiv |J|(-1 \text{ V})/|J|(1 \text{ V})$ increase with n from near unity to a maximum value of 37–50 for $n = 3$. These diodes with conjugated backbone perform remarkably well, with RR values of just a factor 2 smaller than the well-known molecular diode of the form Ag-S(CH₂)₁₁Fc//Ga₂O₃/EGaIn ($RR = 1.0 \times 10^2$) in which the HOMO is localized on the Fc unit in van der Waals contact with the top electrode and is isolated from the bottom electrode

by the insulating alkyl chain. The diodes reported here perform well compared against other well-known diodes (see [ref. 38] for an extensive review), but are inferior to diodes based on two Fc units.^[39] Due to this asymmetry, at positive bias, the HOMO level is outside of the bias window and the charge needs to traverse the junction via coherent tunneling. At negative bias, the HOMO of Fc can participate in charge transport and provides a hopping site for holes.^[40] By replacing the insulating alkyl chain with a conjugated OPE backbone, one could argue that the molecular diode would cease to operate well due to the expected delocalization of the HOMO over the entire molecule with associated loss of asymmetry. Our DFT calculations, however, show that the HOMO remains localized on the iron atom of the Fc ensuring good performance despite the conjugated OPE backbone. The molecular diodes with $n = 1$ do not rectify significantly likely because the OPE backbone is too short for the charge transport mechanism to switch to hopping at the

negative bias (since coherent tunneling rates increase exponentially with decreasing d).^[41]

Figure 3c,d shows the current decay plots as a function of the molecular length d_{mol} (the distance between the hydrogen atom in the thiol group and the furthest carbon atom in the Fc in CPK molecular models) at $V = +1.0$ V and -1.0 V which we used to determine the tunneling decay coefficient β by fitting the data to

$$J = J_0 e^{-d_{\text{mol}}\beta} \quad (4)$$

where J_0 is the pre-exponential factor. Because through-bond, rather than through-space, is the dominant tunneling pathway in molecular junctions,^[42–46] we used d_{mol} , not d_{SAM} , as the tunneling distance in this study. At positive bias, the HOMO does not enter the bias window and the mechanism of charge transport is off-resonant tunneling (see the energy-level diagram later in Figure 7) with $\beta = 0.44 \pm 0.02 \text{ \AA}^{-1}$ for S-OPE_nFc. This value of β is slightly larger than the range of previously reported values for conjugated molecular wires (0.2–0.3 \AA^{-1}) but lower than that for aliphatic wires (0.8 \AA^{-1}). Remarkably, the value of $\beta = 0.29 \pm 0.08 \text{ \AA}^{-1}$ for S-CH₂-OPE_nFc SAMs is smaller than that of S-OPE_nFc, possibly due to the involvement of LUMO which will be discussed in detail later. At -1.0 V, β becomes very small for both series which indicates that incoherent tunneling dominates the mechanism of charge transport. The transition from coherent to incoherent tunneling has been observed for molecular wires of 3–4 nm length,^[47,48] but in our case, the Fc unit facilitates hole injection resulting in incoherent tunneling at relatively short molecular lengths in only one direction of bias.^[9,40] For these reasons, we conclude that the shortest molecules in our study operate in the coherent tunneling regime, while for molecules with $n = 2$ and 3, incoherent transport is important at negative bias. To shed more light on the mechanism of charge transport, we conducted temperature-dependent $J(V)$ measurements.

2.3. Charge transport in the Marcus Inverted Region

To investigate the temperature dependence of the charge transport properties of our junctions, we stabilized EGaIn in a microfluidic channel to enable $J(V)$ measurements in a vacuum and at low temperatures^[49] (see Section S9, Supporting Information for the detailed fabrication procedure). The complete data sets recorded from all junctions are summarized in Figure S22–S27, Supporting Information. The values of J and RR of the junctions are within one standard deviation of those from the same junctions using cone-shaped EGaIn tips (Figure 3). The $J(V)$ data for junctions with S-CH₂-OPE_nFc and S-OPE_nFc with $n = 1$ are independent of T , but junctions with $n = 2$ and 3 are dependent on T . Interestingly, for junctions with S-CH₂-OPE_nFc the value of E_a strongly depends on the applied V while in junctions with S-OPE_nFc the value of E_a is independent of V .

To elucidate this difference in the temperature dependence in more detail, we determined the value of E_a by plotting the data in Arrhenius plots for each V (see Figure S22–S27, Supporting Information for all Arrhenius plots) and fitting the data to the Arrhenius equation

$$J = J_0 e^{\frac{-E_a}{k_B T}} \quad (5)$$

Figure 4 shows E_a plotted against V (the currents from -0.2 V to $+0.2$ V are lower than the detection limit of the setup and are therefore omitted). For S-OPE₁Fc ($T = 180 - 270$ K) and S-CH₂-OPE₁Fc ($T = 240 - 300$ K), the charge transport process is essentially activationless ($E_a \approx 0$ meV) over the entire bias window, indicating that coherent tunneling dominates the mechanism of charge transport. For S-OPE₂Fc ($E_a = 18.8 \pm 8.5$ meV, $T = 150 - 320$ K) and S-OPE₃Fc ($E_a = 88.1 \pm 6.1$ meV, $T = 150 - 300$ K), E_a is independent of V at negative bias. This indicates incoherent tunneling in Marcus normal region is the primary charge transport mechanism in these junctions. Hence, intramolecular

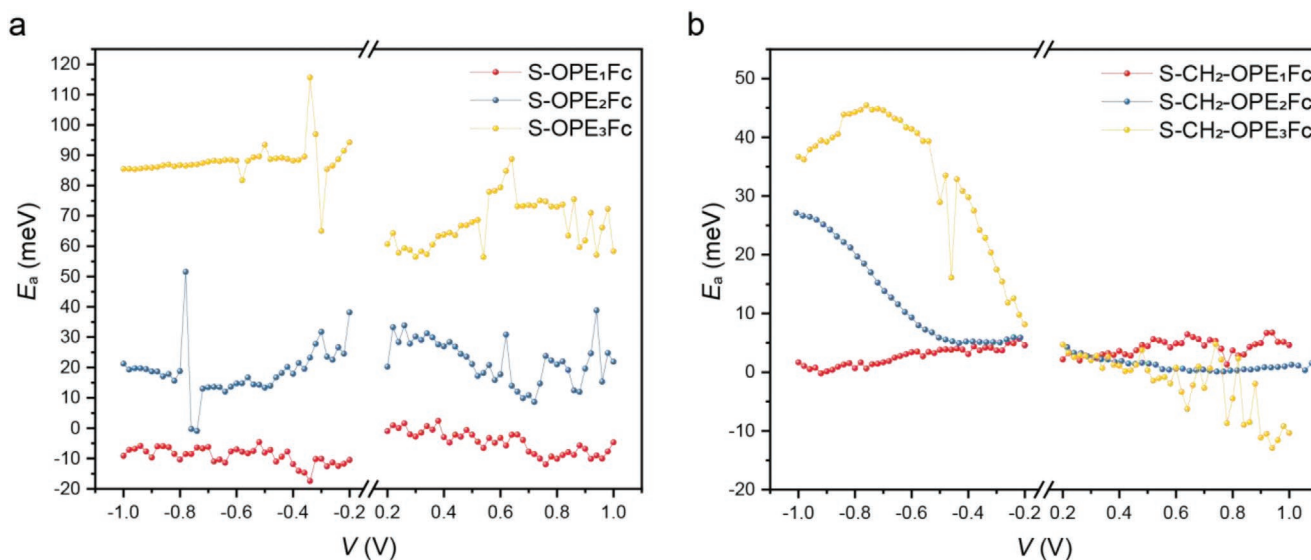


Figure 4. The activation energy E_a as a function of V for a) S-OPE_nFc and b) S-CH₂-OPE_nFc series. For each type of junction, three data sets are given in the Supporting Information.

Table 2. Summary of the fitting parameters for S-OPE_nFc and S-CH₂-OPE_nFc junctions.

SAM	A	W	λ [eV]	C _c [F]
S-CH ₂ -OPE ₁ Fc	-0.40	0.681	0.040	8.96 × 10 ⁻²⁰
S-CH ₂ -OPE ₂ Fc	-0.26	0.681	0.060	8.32 × 10 ⁻²⁰
S-CH ₂ -OPE ₃ Fc	-0.15	0.681	0.12	7.68 × 10 ⁻²⁰

orbital gating does not occur in these molecules (see ref. [9]), as discussed below. For S-OPE₃Fc the value of E_a is approximately five times larger than for S-OPE₂Fc even though both SAMs have very similar δE_{ME} and similar structures (and therefore similar λ). This increase of E_a with molecular length is perhaps even counterintuitive as, in general, long-conjugated molecules can delocalize charges better than short-conjugated molecules. We attribute this increase of E_a value in S-OPE_nFc junctions to the increase in the tunnel distance d (and associated decrease in molecule-electrode coupling strength γ , see below in Table 2) resulting in a substantial decrease in coherent tunneling rates: for junctions with $n = 1$ coherent tunneling dominates but for junctions with $n = 2$ and 3 coherent tunneling rates decrease and therefore incoherent tunneling increasingly dominates the mechanism of charge transport.

For S-CH₂-OPE₂Fc and S-CH₂-OPE₃Fc, E_a is close to zero at positive bias, indicating a coherent tunneling mechanism. Above +0.6 V the E_a for S-CH₂-OPE₃Fc appears to be negative, which, upon careful observation in the Arrhenius plot (Figure S27, Supporting Information), mainly comes from the results at >220K. This behavior has been reported for junctions with ferrocene-functionalized alkanethiolate junctions because 1) the SAMs prefer a more vertical configuration and increase the tunneling barrier width and 2) the repulsive force between ferrocenium cations leads to poor contact with the top electrode.^[50] Although we cannot be certain what causes a negative E_a , negative E_a has been observed before in other junctions^[51] which could involve re-organization of the SAM induced by electrostatic repulsion (as confirmed by cyclic voltammetry discussed earlier and observed by others^[52]) and could explain our observations. Recently, Marcus and coworkers^[53] suggested that a large change in entropy could result in negative E_a . We note that the values of E_a reported here are lower than those typically obtained from wet electrochemical experiments because molecular junctions lack electrolyte. Hence, the outer sphere reorganization energy is negligible and E_a is dominated by the innersphere contribution. Interestingly, a bell-shaped E_a versus V curve is observed at negative bias which is discussed in detail in the next section.

2.4. Numerical Modeling

Equation (3) was used to fit the E_a versus V data shown in Figure 4. As shown in Figure 4a, E_a in the S-OPE_nFc series is independent of the applied bias, as expected for the normal Marcus region. Further, there is no statistically significant change in E_a as a function of V for positive biases in the S-CH₂-OPE_nFc series. Therefore, the Migliore and Nitzan's model (Equations 3) was used to fit the data shown in Figure 4b

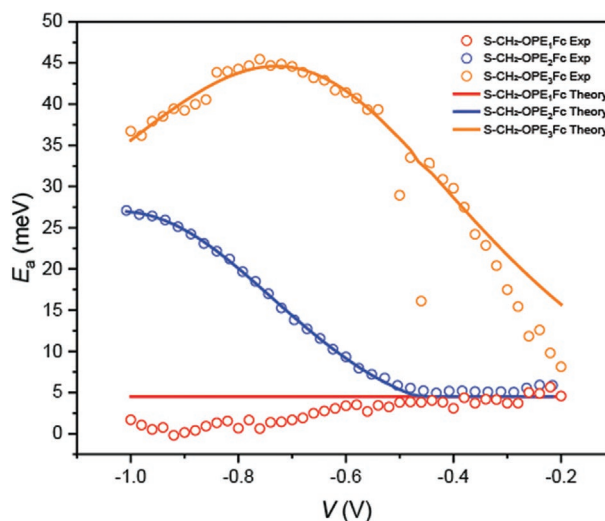


Figure 5. E_a versus V curves of junction Au/S-CH₂-OPE_nFc//GaO_x/EGaIn along with fits to the model by Migliore and Nitzan as explained in the main text.

for negative biases. As stated previously, this model for E_a is dependent of V_g , the intramolecular gating voltage. This gating voltage does not come directly from the applied bias voltage. It comes from the charge build-up in the molecule. Therefore, V_g can be written as, $V_g = \frac{Q(V_b)}{C_c}$. Here, C_c represents the capacitance and the charge, $Q(V_b)$, on the molecule is dependent on the applied bias voltage. To represent the charging on the molecule, we used the function given by Equation (6), where A is the center of the charging function and W is the width.

$$Q(V) = \frac{1}{1 + \exp\left(\frac{V - A}{W}\right)} \quad (6)$$

Figure 5 shows the fits to the behavior of the activation energy as a function of applied bias for the S-CH₂-OPE_nFc series. For S-CH₂-OPE₃Fc, E_a continuously increases to a maximum ≈ -0.7 V and decreases at higher bias. For S-CH₂-OPE₂Fc, the activation energy only starts increasing after ≈ -0.5 V and keeps rising to -1.0 V, while no significant voltage-dependence is observed for the S-CH₂-OPE₁Fc junction. The model accurately portrays the change in E_a for S-CH₂-OPE₃Fc and S-CH₂-OPE₂Fc, while for the S-CH₂-OPE₁Fc the model shows a straight line at 0 meV, indicating a charge transport process dominated by coherent tunneling. The parameters used for these fits are listed in Table 2 and shown in Figure 6.

Figure 6a shows that ΔE decreases with increasing n due to the reducing HOMO-LUMO gap with n shown in Table 1. The values of λ are close to those predicted by theory^[56] (and experimentally observed excitations^[57]), but increase with n (Figure 6b), which suggests that either the shape of the parabolas becomes steeper or the reaction coordinates of the two parabolas move further away from each other, counteracting the decreasing ΔE . Other factors such as gating via applied electric field or the presence of a twist angle between Fc and OPE, or between OPE units, could also affect λ . The increasing

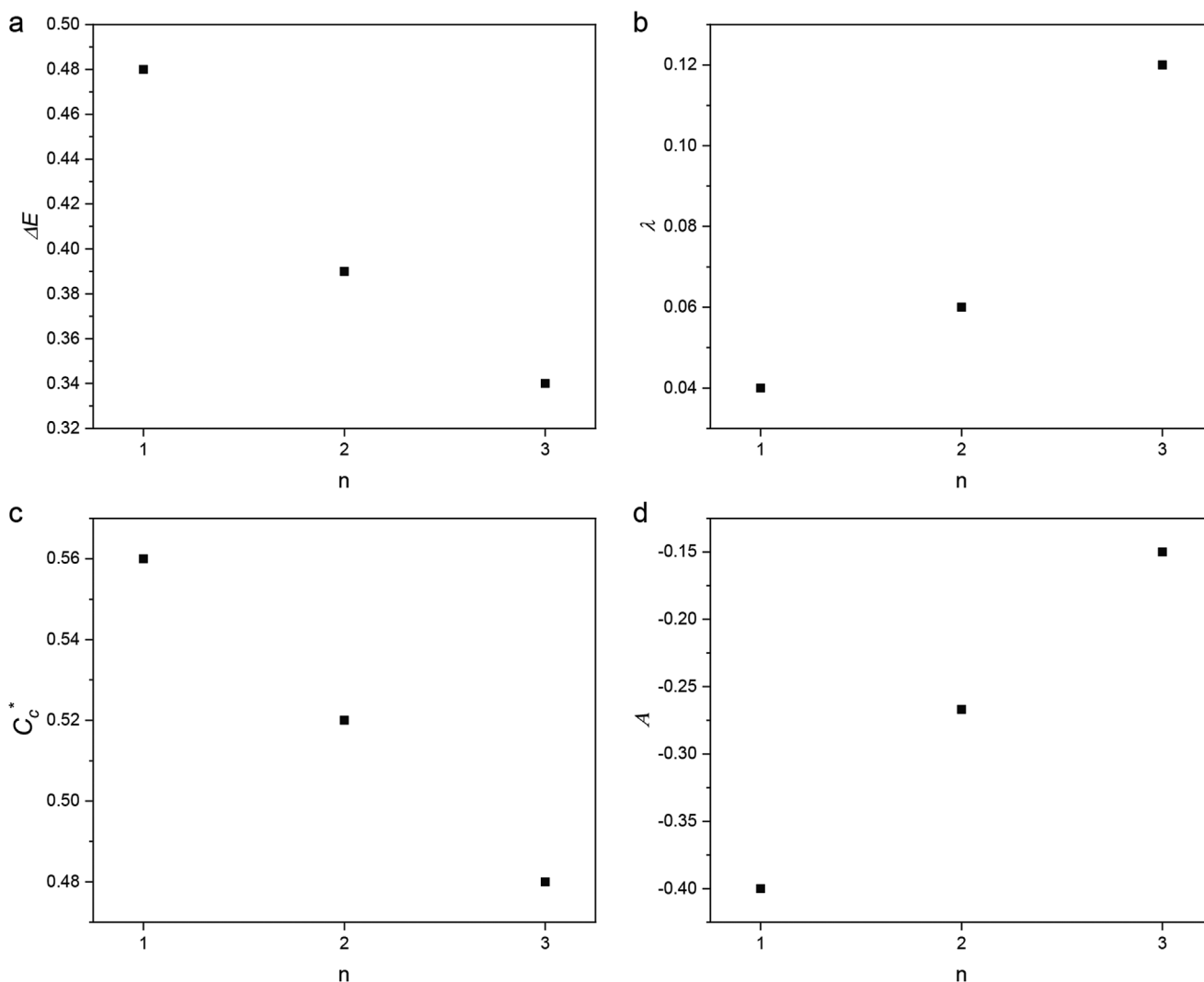


Figure 6. The parameters used in the fitting of E_a as a function of V for junction Au/S-CH₂-OPE_nFc//GaO_x/EGaIn as a function of n : a) ΔE , b) λ , c) C_c , and d) A (with distribution width $W = 0.681$ V for all junctions).

λ should contribute to the higher E_a values for S-CH₂-OPE₃Fc than S-CH₂-OPE₂Fc at negative bias. The decrease of the center voltage of the charge distribution A with increasing n (Figure 6d) is consistent with the increase of η for longer molecules (Table 2). Figure 6c shows a slight decrease of C_c with increasing n , which increases the effective V_g . In addition, although the coupling between the Fc and the adjacent OPE changes slightly with n , the larger the aromatic group the more charge it will be able to host for a given V , resulting in an increase of Q with n . The combined effect of Q and C_c gives larger V_g for S-CH₂-OPE₃Fc than S-CH₂-OPE₂Fc, making the required V lower for the system to enter the MIR.

To illustrate the charge transport mechanisms in these junctions, the energy level diagrams at both positive and negative bias are shown in Figure 7. Figure 2f shows that the HOMOs of the molecules are located at the Fc groups while the LUMOs are more delocalized over the molecule. At zero bias for a given molecule, E_{HOMO} is 0.7–0.8 eV lower than the E_F , and E_{LUMO} is more than 2 eV higher than the Fermi levels (Table 1). Figure 7a

shows the energy level alignment of the junctions at +1 V bias. Neither the HOMO nor the LUMO is in the conduction window and the electrons transport by coherent tunneling. The small E_a values for S-OPE₂Fc (≈ 20 meV) and S-OPE₃Fc (≈ 60 meV) suggest that incoherence is present in these junctions.

Figure 7b shows that when -1 V bias is applied to the junction, the HOMO enters the conduction window. The Fc group can be charged due to its tendency to lose one electron to form ferrocenium (Fc⁺). This charged Fc⁺ can reduce the energy level of the LUMO to shift it inside the conduction window. The decrease in HOMO–LUMO gap makes the charge transfer between Fc and OPE more exergonic, shifting the tunneling mechanism into MIR (red parabola in Figure 1c). In S-CH₂-OPE₂Fc and S-CH₂-OPE₃Fc, the weak coupling between OPE and Au allows the electrons to localize on the LUMO. For these SAMs, the model of Migliore et al.^[23] accurately predicts the bell-shaped curve of E_a in Figure 4b. The intramolecular gating effect pushes the charge transport mechanism into MIR. On the contrary, the stronger coupling between molecules and the

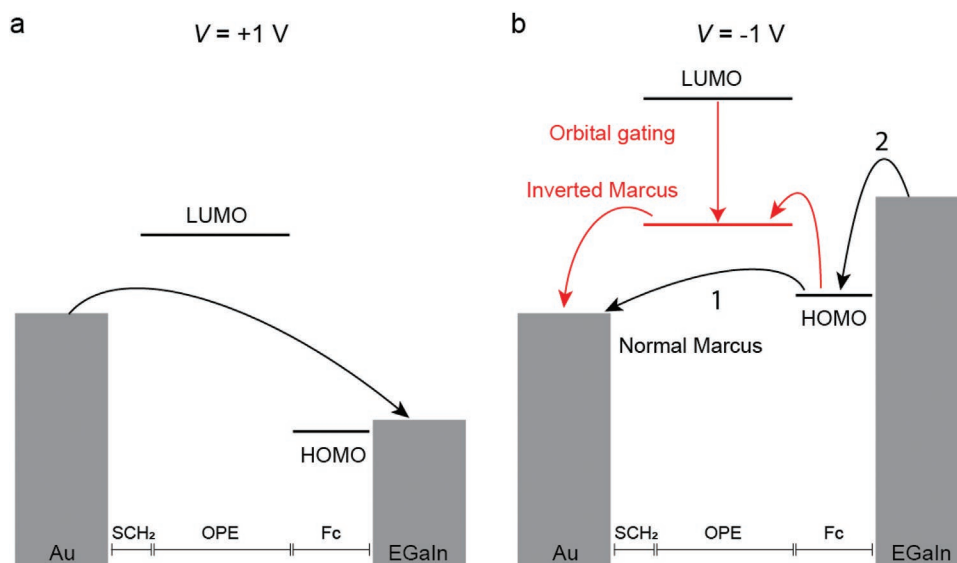


Figure 7. Energy level diagrams of junctions at a) +1.0 V bias and b) –1.0 V bias, where the black arrows indicate the electron transport, and the red arrow indicates the shift of LUMO level due to the intramolecular gating effect in S-CH₂-OPE_nFc opening up a new electron transfer pathway indicated with red curved arrows. Note, the arrows indicate electron transfer pathways; in this notation, an electron tunnels first out of the HOMO (black arrow 1) to leave behind a hole.

Au electrode for S-OPE₂Fc and S-OPE₃Fc precludes the gating effect of Fc⁺. The HOMO remains weakly coupled to both electrodes, making incoherent tunneling through HOMO the dominating charge transport mechanism.

3. Conclusions

In this study, we have shown that the mechanism of charge transport can be deliberately switched between the normal and Marcus Inverted regions by controlling the molecule–electrode coupling strength in a series of molecules. We can change the strength of the intramolecular gating by adjusting the length of the molecular wire, only when the molecules are both >2 nm long and weakly coupled to the electrode, which shifts the charge transport mechanism from the normal Marcus regime to the Marcus Inverted region. The coupling strength between the donor Fc and acceptor OPE, and the coupling strength between the molecule and the electrodes, provide two distinct parameters to control intramolecular orbital gating which in turn allows us to control the charge transport mechanism. This ability to push the junction in and out of the activationless Marcus Inverted region could potentially improve the energy efficiency of electric circuits.

Supporting Information

Supporting Information is available from the Wiley Online Library or from the author.

Acknowledgements

The authors acknowledged the National Research Foundation (NRF) for supporting this research under the Prime Minister's Office, Singapore,

under its Medium-Sized Centre Programme and the Competitive Research Programme (CRP; NRF-CRP17-2017-08). D.T. thanks Science Foundation Ireland (SFI) for support (awards no. 15/CDA/3491 and 12/RC/2275_P2), and for computing resources at the SFI/Higher Education Authority Irish Center for High-End Computing (ICHEC). L.W. acknowledges the support of the Natural Science Foundation of China (NSFC 21805144) and the Ningbo Municipal Government (NSF 2019A610138). The spectroscopy was recorded at the Soft X-ray Spectroscopy beamline at the Australian Synchrotron, part of ANSTO.

Conflict of Interest

The authors declare no conflict of interest.

Data Availability Statement

The data that support the findings of this study are available from the corresponding author upon reasonable request.

Keywords

charge transport, EGaIn, molecular electronics, Marcus Inverted Region, self-assembled monolayers

Received: June 8, 2022
Revised: October 20, 2022
Published online:

- [1] P. Li, Z.-H. Lu, *Small Sci.* **2021**, *1*, 2000015.
- [2] M. Kaneko, T. Okada, T. Okada, M. Kaneko, Eds., *Springer Series in Materials Science*, Springer, Berlin, Heidelberg **2009**, pp. 37–65.
- [3] B. A. Johnson, A. M. Beiler, B. D. McCarthy, S. Ott, *J. Am. Chem. Soc.* **2020**, *142*, 11941.

- [4] P. R. Bueno, J. J. Davis, *Chem. Soc. Rev.* **2020**, *49*, 7505.
- [5] M. A. O'Neill, J. K. Barton, G. B. Schuster, Ed., *Topics in Current Chemistry*, Springer, Berlin, Heidelberg **2004**, pp. 67–115.
- [6] K. Wang, E. Meyhofer, P. Reddy, *Adv. Funct. Mater.* **2020**, *30*, 1904534.
- [7] L. Chen, A. Feng, M. Wang, J. Liu, W. Hong, X. Guo, D. Xiang, *Sci. China Chem.* **2018**, *61*, 1368.
- [8] Z. Liu, S. Ren, X. Guo, *Top. Curr. Chem.* **2017**, *375*, 56.
- [9] L. Yuan, L. Wang, A. R. Garrigues, L. Jiang, H. V. Annadata, M. A. Antonana, E. Barco, C. A. Nijhuis, *Nat. Nanotechnol.* **2018**, *13*, 322.
- [10] H. Kang, G. D. Kong, S. E. Byeon, S. Yang, J. W. Kim, H. J. Yoon, *J. Phys. Chem. Lett.* **2020**, *11*, 8597.
- [11] R. A. Marcus, *Discuss. Faraday Soc.* **1960**, *29*, 21.
- [12] Y. Han, C. Nickle, M. S. Maglione, S. K. Karuppanan, J. Casado-Montenegro, D.-C. Qi, X. Chen, A. Tadich, B. Cowie, M. Mas-Torrent, C. Rovira, J. Cornil, J. Veciana, E. Barco, *Adv. Sci.* **2021**, *8*, 2100055.
- [13] A. Atxabal, T. Arnold, S. Parui, S. Hutsch, E. Zuccatti, R. Llopis, M. Cinchetti, F. Casanova, F. Ortmann, L. E. Hueso, *Nat. Commun.* **2019**, *10*, 2089.
- [14] R. Landauer, *IBM J. Res. Dev.* **1957**, *1*, 223.
- [15] E. G. Emberly, G. Kirczenow, *Phys. Rev. B* **2000**, *61*, 5740.
- [16] L. A. Zotti, T. Kirchner, J.-C. Cuevas, F. Pauly, T. Huhn, E. Scheer, A. Erbe, *Small* **2010**, *6*, 1529.
- [17] J. A. Fereiro, X. Yu, I. Pecht, M. Sheves, J. C. Cuevas, D. Cahen, *Proc. Natl. Acad. Sci.* **2018**, *115*, E4577.
- [18] R. A. Marcus, *J. Chem. Phys.* **1956**, *24*, 966.
- [19] R. A. Marcus, *J. Chem. Phys.* **1957**, *26*, 867.
- [20] A. Migliore, A. Nitzan, *ACS Nano* **2011**, *5*, 6669.
- [21] A. Migliore, A. Nitzan, *J. Am. Chem. Soc.* **2013**, *135*, 9420.
- [22] C. Jia, A. Migliore, N. Xin, S. Huang, J. Wang, Q. Yang, S. Wang, H. Chen, D. Wang, B. Feng, Z. Liu, G. Zhang, D.-H. Qu, H. Tian, M. A. Ratner, H. Q. Xu, A. Nitzan, X. Guo, *Science* **2016**, *352*, 1443.
- [23] A. Migliore, P. Schiffr, A. Nitzan, *Phys. Chem. Chem. Phys.* **2012**, *14*, 13746.
- [24] H. Kang, G. D. Kong, H. J. Yoon, *J. Phys. Chem. Lett.* **2021**, *12*, 982.
- [25] R. C. Chiechi, E. A. Weiss, M. D. Dickey, G. M. Whitesides, *Angew. Chem., Int. Ed.* **2008**, *47*, 142.
- [26] C.-P. Chen, W.-R. Luo, C.-N. Chen, S.-M. Wu, S. Hsieh, C.-M. Chiang, T.-Y. Dong, *Langmuir* **2013**, *29*, 3106.
- [27] L. Herrer, A. González-Orive, S. Marqués-González, S. Martín, R. J. Nichols, J. L. Serrano, P. J. Low, P. Cea, *Nanoscale* **2019**, *11*, 7976.
- [28] C. A. Nijhuis, W. F. Reus, G. M. Whitesides, *J. Am. Chem. Soc.* **2009**, *131*, 17814.
- [29] L. Jiang, L. Yuan, L. Cao, C. A. Nijhuis, *J. Am. Chem. Soc.* **2014**, *136*, 1982.
- [30] E. Laviron, *J. Electroanal. Chem. Interfacial Electrochem.* **1979**, *100*, 263.
- [31] N. Nerngchamnong, D. Thompson, L. Cao, L. Yuan, L. Jiang, M. Roemer, C. A. Nijhuis, *J. Phys. Chem. C* **2015**, *119*, 21978.
- [32] E. Laviron, *J. Electroanal. Chem. Interfacial Electrochem.* **1979**, *101*, 19.
- [33] O. Alévêque, P.-Y. Blanchard, C. Gautier, M. Dias, T. Breton, E. Levillain, *Electrochem. Commun.* **2010**, *12*, 1462.
- [34] J. Trasobares, J. Rech, T. Jonckheere, T. Martin, O. Aleveque, *Nano Lett.* **2017**, *17*, 3215.
- [35] D. Thompson, C. A. Nijhuis, *Acc. Chem. Res.* **2016**, *49*, 2061.
- [36] N. Nerngchamnong, L. Yuan, D.-C. Qi, J. Li, D. Thompson, C. A. Nijhuis, *Nat. Nanotechnol.* **2013**, *8*, 113.
- [37] X. Chen, H. Hu, J. Trasobares, C. A. Nijhuis, *ACS Appl. Mater. Interfaces* **2019**, *11*, 21018.
- [38] R. M. Metzger, *Chem. Rev.* **2003**, *103*, 3803.
- [39] X. Chen, M. Roemer, L. Yuan, W. Du, D. Thompson, E. del Barco, C. A. Nijhuis, *Nat. Nanotechnol.* **2017**, *12*, 797.
- [40] C. A. Nijhuis, W. F. Reus, J. R. Barber, M. D. Dickey, G. M. Whitesides, *Nano Lett.* **2010**, *10*, 3611.
- [41] C. Joachim, M. A. Ratner, *Proc Natl Acad Sci USA* **2005**, *102*, 8801.
- [42] S. K. Karuppanan, R. R. Pasula, T. S. Heng, J. Ding, X. Chi, E. D. Barco, S. Roche, X. Yu, N. Yakovlev, S. Lim, C. A. Nijhuis, *J. Phys. Mater.* **2021**, *4*, 035003.
- [43] W. Du, Y. Han, H. Hu, H.-S. Chu, H. V. Annadata, T. Wang, N. Tomczak, *Nano Lett.* **2019**, *19*, 4634.
- [44] P. Gehring, J. M. Thijssen, H. S. J. van der Zant, *Nat. Rev. Phys.* **2019**, *1*, 381.
- [45] M. Gilbert, B. Albinsson, *Chem. Soc. Rev.* **2015**, *44*, 845.
- [46] J. Liu, X. Huang, F. Wang, W. Hong, *Acc. Chem. Res.* **2019**, *52*, 151.
- [47] Q. Lu, K. Liu, H. Zhang, Z. Du, X. Wang, F. Wang, *ACS Nano* **2009**, *3*, 3861.
- [48] X. Yao, X. Sun, F. Lafolet, J.-C. Lacroix, *Nano Lett.* **2020**, *20*, 6899.
- [49] A. Wan, L. Jiang, C. S. S. Sangeeth, C. A. Nijhuis, *Adv. Funct. Mater.* **2014**, *24*, 4442.
- [50] H. Jeong, Y. Jang, D. Kim, W.-T. Hwang, J.-W. Kim, T. Lee, *J. Phys. Chem. C* **2016**, *120*, 3564.
- [51] F. A. Alami, S. Soni, A. Borrini, C. A. Nijhuis, *ECS J. Solid State Sci. Technol.* **2022**, *11*, 055005.
- [52] S. Ye, Y. Sato, K. Uosaki, *Langmuir* **1997**, *13*, 3157.
- [53] J. K. Sowa, R. A. Marcus, *Chem. Phys.* **2021**, *154*, 034110.
- [54] Y. Han, C. Nickle, Z. Zhang, H. P. A. G. Astier, T. J. Duffin, D. Qi, Z. Wang, E. del Barco, D. Thompson, C. A. Nijhuis, *Nat. Mater.* **2020**, *19*, 843.
- [55] A. R. Garrigues, L. Yuan, L. Wang, E. R. Mucciolo, D. Thompon, E. del Barco, C. A. Nijhuis, *Sci. Rep.* **2016**, *6*, 26517.
- [56] S. Ghosh, S. Hammes-Schiffer, *J. Phys. Chem. Lett.* **2015**, *6*, 1.
- [57] N. P. De Leon, Liang Wenjie, Q. Gu, H. Park, *Nano Lett.* **2008**, *8*, 2963.